



FRANCE_CANNES 15-18 SEPT 25

THE FUTURE IS SCIENCE

ifsc2025.com



SOCIÉTÉ FRANÇAISE DE COSMÉTOLOGIE

IFSCC 2025 full paper (IFSCC2025-430)

"Preparation and Properties of Recombinant Collagen Microspheres Loaded with Epigallocatechin-3-Gallate for Photodamage Repair"

Chanhua Zhou¹, Yadong Huang¹, Ziyi Huang^{1,*} and Qiaoxue Xiao¹¹ R&D Department, Tyran (Guangzhou) Biotechnology Co., Ltd., Guangzhou, China

1 Introduction

Skin photoaging, primarily induced by ultraviolet (UV) radiation, is characterized by excessive reactive oxygen species (ROS) generation, collagen degradation, and upregulated matrix metalloproteinase (MMP) activity^[1]. Chronic UV exposure causes structural deterioration of the dermal layer, manifesting as loss of skin elasticity, wrinkle formation, and impaired barrier function^[2]. Current topical collagen-based therapies have attracted significant attention due to their potential to directly replenish extracellular matrix components^[3]. However, conventional recombinant human collagen (RHC) exhibits markedly limited bioavailability owing to its large molecular weight, which impedes stratum corneum penetration and subsequent delivery to dermal action sites^[4]. In contrast, although antioxidants such as vitamin C and epigallocatechin gallate (EGCG) can suppress MMP activity through ROS scavenging, their clinical translation remains challenging due to inherent chemical instability and suboptimal transdermal efficiency^[5,6]. These limitations underscore the critical need to develop novel delivery systems capable of simultaneously overcoming the transdermal barrier for macromolecules while addressing the stability deficiencies of small molecules, thereby enhancing therapeutic efficacy in photoaging intervention.

Notably, anti-aging concepts and sunscreen products formulated with natural plant ingredients are increasingly favored by consumers. Among these, natural plant polyphenols exhibit strong antioxidant properties, along with whitening, anti-inflammatory, and UV protection effects, making them key components in many anti-aging products^[6]. Epigallocatechin gallate (EGCG) is a significant polyphenol found in green tea, known for its potent antioxidant and anti-inflammatory properties that can mitigate oxidative damage induced by ultraviolet radiation^[7]. The molecular mechanisms underlying its action involve direct scavenging of reactive oxygen species (ROS)^[8], inhibition of the NF-κB signaling pathway^[9], and downregulation of MMP-1/MMP-3 expression^[10]. However, EGCG demonstrates significant limitations in physiological environments, where it undergoes rapid

oxidative polymerization - particularly under alkaline conditions ($\text{pH} > 7$) or elevated temperatures - resulting in substantial loss of bioactivity^[5]. Furthermore, in vitro studies have revealed that supraphysiological concentrations of EGCG ($> 50 \mu\text{M}$) may paradoxically induce oxidative stress and exhibit cytotoxic effects on fibroblasts^[11]. These inherent physicochemical instability issues and concentration-dependent toxicity profile critically restrict its potential as a monotherapeutic agent in topical formulations.

Various nano-delivery systems have been developed to enhance the stability and bioavailability of EGCG, including liposomes^[12], nanoemulsion systems^[13], nanoparticles^[14], and others. By encapsulating EGCG within these carriers, the inherent toxicity of EGCG can be reduced while its bioavailability and stability are improved. Recent investigations have revealed that polyphenolic compounds (e.g., tannic acid, EGCG) can spontaneously self-assemble with proteins through non-covalent interactions (hydrogen bonding and π - π stacking) to form core-shell nanoparticles. Numerous experiments have confirmed that self-assembled systems exhibit greater stability and antioxidant properties than free systems^[6]. In particular, bionanomaterials formed through polyphenol-protein assembly combinations have been extensively developed^[15]. Compared to other nano-carriers such as liposomes and polymeric nanoparticles, the polyphenol-protein assembled nanosystem exhibits excellent biocompatibility, biodegradability, and abundant availability.

In this study, we developed a facile one-step self-assembly strategy leveraging polyphenol-protein interactions to fabricate EGCG-RHC nanospheres (EGCG-RHC SNs), which were systematically evaluated in a UVB-induced cell photoaging model. The proline/hydroxyproline-rich domains in RHC offer multiple binding sites for EGCG, enabling the formation of stable self-assembled nanoparticles through optimized intermolecular interactions. This innovative approach not only employed steric hindrance effects to protect EGCG from oxidative degradation but also achieved precise control over nanoparticle size ($< 100 \text{ nm}$). Consequently, this strategy established a dual-functional delivery system that addressed the inherent limitations of both EGCG and RHC, markedly improving EGCG's chemical stability while boosting RHC's skin permeability. In UV-induced damage models, EGCG-RHC SNs demonstrated potent ROS scavenging capacity and promoted macrophage polarization towards the M2 anti-inflammatory phenotype, exhibiting dual antioxidant and anti-inflammatory efficacy. Functional assays including CCK-8, colony formation, wound healing, and JC-1 staining further revealed that EGCG-RHC SNs enhanced cell viability, restored proliferative/migratory capacities in photodamaged cells, and alleviated UV-induced cellular damage. Moreover, EGCG-RHC SNs represent a safe and reliable sustained-release nanodelivery system. This study not only provided a robust theoretical foundation for the application of plant polyphenols and RHC in skin photoaging but also established a paradigm for the development of synergistic biomaterial-based therapeutic systems.

2 Materials and Methods

2.1 Materials

Recombinant human type III collagen was obtained from China. Epigallocatechin gallate (EGCG, purity $\geq 98\%$) was commercially sourced. CCK-8 detection reagent, DAPI nuclear

stain, DCFH-DA fluorescent probe, DMEM medium, and RPMI 1640 medium were procured from scientific suppliers. Fetal bovine serum (FBS) and fluorescein isothiocyanate (FITC) were obtained through standard laboratory channels. DAB chromogenic substrate kit was acquired from biochemical providers. All materials were used according to standardized experimental protocols without brand-specific indications.

2.2 Preparation of EGCG-RHC SNs

EGCG-RHC nanoparticles were synthesized through stoichiometric coordination (1:1 mass ratio) between RHC and EGCG (0.8 mg/mL) in saline under magnetic agitation (1000 rpm, 5 min). Post-centrifugation purification and lyophilization yielded stable nanosphere formulations. For fluorescent tracking, covalent conjugation of FITC with RHC was achieved via 12-hour cold incubation (4°C), followed by membrane dialysis to remove unbound fluorophores, producing FITC-tagged nanoparticles (FITC-EGCG-RHC SNs) and labeled RHC controls. Characterization of EGCG-RHC SNs

2.2.1 Determination of Z-Average, Zeta potential and PDI

The EGCG-RHC SNs suspension was diluted threefold with saline prior to measurements. The average particle size (Z-Average), zeta potential, and polydispersity index (PDI) were measured using dynamic light scattering (DLS) at 25°C.

2.2.2 Morphology of EGCG-RHC SNs

The morphological characteristics of EGCG-RHC SNs were characterized using scanning electron microscopy (SEM), transmission electron microscopy (TEM), and atomic force microscopy (AFM). For SEM analysis, lyophilized samples were mounted on conductive substrates, sputter-coated with gold nanoparticles, and imaged at 10 kV accelerating voltage. TEM specimens were prepared by depositing saline-diluted suspensions (10:1) onto copper grids followed by ambient drying. Particle size distribution was quantified using digital image analysis software. AFM characterization involved depositing 5 µL diluted samples on atomically smooth substrates, with surface topography analyzed through dedicated scanning probe analysis software.

2.2.3 Fourier Transform Infrared Spectroscopy (FTIR) analysis.

Fourier-transform infrared (FTIR) spectroscopy was employed to analyze structural changes in EGCG-RHC SNs through comparative examination of characteristic absorption bands among pure EGCG, RHC, and their complex. Lyophilized nanoparticles (1 mg) were homogenized with potassium bromide (KBr) at 1:150 (w/w) ratio and compressed into transparent pellets. Spectral data collection was performed using an FTIR spectrometer with 2 cm⁻¹ resolution across the 4000-700 cm⁻¹ range. Secondary structural interpretation was conducted using specialized spectral processing software.

2.2.4 Molecular Docking

Molecular docking simulations were conducted to elucidate the interaction mechanisms between EGCG and RHC. The RHC crystal structure (PDB ID: 6A0A) was obtained from the Protein Data Bank, while the EGCG ligand (CAS: 989-51-5) was retrieved from PubChem (National Library of Medicine, USA). Preprocessing of both ligand and receptor structures, including hydrogenation and charge assignment, was performed using AutoDock Tools. Docking simulations were executed in PyRx-Vina, followed by selection of the optimal binding

pose based on minimal binding energy.

2.2.5 Ultraviolet Extinction

EGCG (0.8 mg/mL) was combined with graded concentrations of RHC solution under vortex agitation (1000 rpm, 5 min). The resultant mixtures underwent centrifugation (12,000 rpm, 10 min, 4°C) to separate unbound components. Pelleted complexes were subjected to triple saline washing and reconstituted to initial volume for ultraviolet-visible (UV-Vis) spectroscopic characterization, with full-wavelength scanning conducted from 200 nm to 500 nm using a double-beam spectrophotometer.

2.2.6 In vitro extended release assay

Lyophilized EGCG-RHC SNS (50 mg) were homogenized in 50 mL saline under continuous magnetic agitation (25°C). At predetermined intervals (2, 4, 6, 8, 10, 16 h), 500 µL aliquots were withdrawn and immediately replenished with equal volumes of fresh saline. The collected samples were centrifuged (12,000 rpm, 10 min, 4°C), and the absorbance value of the supernatant was measured in the range of 200-500 nm using a spectrophotometer (UV-2600) to calculate the concentration of free EGCG in the solution, and the cumulative rate of release of EGCG was calculated according to the following formula:

$$Q = \frac{(V_1 \sum \rho_i - 1 + V_2 \rho_i) \times 10^{-3}}{1000 m s} \times 100\%$$

Where Q is the cumulative release rate of the system calculated after the i th sampling (%); ρ_i is the mass concentration of drug released at the i th sampling (µg/mL); m is the mass of the dry powder of EGCG-RHC SNS (g); s is the amount of drug loaded V_1 is the volume taken at each sampling (mL); and V_2 is the volume of the buffer solution (mL).

2.2.7 DPPH free-radical scavenging activity assay

The *in vitro* antioxidant capacity of EGCG-RHC SNS was evaluated through 2,2-diphenyl-1-picryl-hydrazyl (DPPH) radical scavenging assays. A 0.1 mmol/L DPPH working solution was prepared by dissolving DPPH powder in anhydrous ethanol under light-protected conditions. Lyophilized EGCG powder, RHC, and EGCG-RHC SNS were individually reconstituted in saline to equivalent mass concentrations. Each sample (100 µL) was mixed with an equal volume of DPPH solution (1:1, v/v) and incubated for 30 min at 25°C in darkness. Absorbance measurements at 517 nm were performed using a UV-2600 spectrophotometer. Trolox served as the positive control; anhydrous ethanol replaced DPPH solution in blank controls. The DPPH scavenging rate (%) was calculated as:

$$\text{DPPH scavenging (\%)} = 1 - \left(\frac{A_1 - A_2}{A_0} \right) \times 100\%$$

where A_1 denotes a free radical ethanol solution of sample and DPPH; A_2 denotes a mixture of sample and ethanol; and A_0 denotes a free radical ethanol solution of phosphate-buffered saline (PBS) and DPPH.

2.3 Evaluate of EGCG-RHC SNS in Vitro

2.3.1 Cytotoxicity Assay

HaCaTs were seeded into 96-well plates at a density of 8×10^3 cells/well and cultured at 37°C with 5% CO₂ until complete adhesion. Cells were subsequently exposed to: (i) Serial

concentrations (0.005-0.04 mg/mL) of RHC, EGCG, and EGCG-RHC SNs (ii) Complete medium alone (negative control) for 24 h. After treatment, 100 µL of CCK-8 working solution (10% v/v in complete medium) was added to each well and incubated under light-protected conditions for 1 h. Absorbance was quantified at 450 nm using a microplate reader.

2.3.2 UVB-induced photoaging cell model

HaCaT cells were plated in 96-well plates at 8×10^3 cells/well and allowed to adhere. Experimental groups received UVB irradiation (120 mJ/cm^2) across varying durations (2-10 min), while controls remained unexposed. Post-irradiation, cells were maintained in complete medium (DMEM + 10% FBS) for 24 h. Cellular viability was assessed via CCK-8 assay: 10% v/v CCK-8 reagent was added to each well, followed by 1 h dark incubation. Absorbance at 450 nm (reference 650 nm) was quantified using a microplate reader.

2.3.3 Cell proliferation assay

HaCaT cells were seeded in 96-well plates at a density of 8,000 cells/well and cultured until adhered. The cells were divided into UV, model, and control groups. After washing with PBS, the UV and model groups were exposed to 120 mJ/cm^2 UV radiation for 6 minutes, while the control group was not irradiated. Following irradiation, all groups were cultured for 24 hours in fresh medium containing the respective samples. CCK-8 solution was then added, and the plate was incubated in the dark for 1 hour. Absorbance at 450 nm was measured using a Microplate Reader to calculate the cell survival rate.

2.3.4 cell clone assay

HaCaT cells were seeded in 6-well plates at a density of 1×10^3 cells/well and cultured until adhesion. The UV and model groups were exposed to 120 mJ/cm^2 UV radiation for 6 minutes, while the control group remained untreated. Cells were washed twice with PBS, and 2 mL of fresh DMEM complete medium containing 0.01 mg/mL of the respective samples was added to the experimental groups. The control and model groups received fresh DMEM complete medium. The cells were incubated at 37°C with 5% CO_2 and fresh medium was replaced every 2 days. When visible cell clones were observed, the incubation was terminated. The cells were washed with PBS, fixed with 1 mL of 4% paraformaldehyde for 15 minutes, and then washed again. Finally, 1 mL of 1% crystal violet staining solution was added to each well, and the cells were stained at room temperature for 30 minutes. After washing and drying, the number of cell clones was counted using an inverted microscope.

2.3.5 cell migration assay

NIH-3T3 cells were seeded in 12-well plates at a density of 2×10^5 cells/well and cultured to >90% confluence. UV-treated groups received 120 mJ/cm^2 UVB irradiation (6 min), with controls remaining unexposed.

2.3.6 Determination of ROS

The in vitro antioxidant capacity of EGCG-RHC SNs was evaluated using 2',7'-dichlorodihydrofluorescein diacetate. Following UVB irradiation and sample treatment, cells were washed twice with PBS and subsequently incubated with 200 µL DCFH-DA solution in the dark at 37°C for 30 min. After removing the culture medium, cells were fixed with 4% paraformaldehyde for 15 min, followed by three PBS washes. Nuclei were counterstained with DAPI reagent for 10 min before final PBS washing. Cell slides were inverted and mounted for

observation of intracellular ROS levels using confocal microscopy .

2.3.7 Mitochondrial membrane potential assay

HaCaT cells were seeded at 2×10^5 cells/well in 24-well plates with glass coverslips and cultured until adherent. Following 6-min UVB irradiation and sample treatment, cells were washed with PBS, fixed with 4% paraformaldehyde for 15 min, and washed three times with PBS. Cells were incubated with 200 μ L JC-1 dye (2 μ M) protected from light for 15 min. After PBS washing, anti-fade mounting medium was applied. Coverslips were inverted onto slides and analyzed for JC-1 fluorescence using a laser scanning confocal microscope .

2.3.8 Macrophage polarization assay

RAW 264.7 cells were seeded at 2×10^5 cells/well in 24-well plates containing glass coverslips and cultured until adherent. After PBS washing, cells were stimulated with 500 μ L LPS (1,000 ng/mL) for 2 h to induce M0-to-M1 macrophage polarization. Subsequently, cells were washed and treated with 0.01 mg/mL test samples in DMEM for 24 h. Following PBS washing, cells were fixed with 4% paraformaldehyde (15 min), permeabilized with 0.5% Triton X-100, and washed again. Macrophages were incubated with CD206 primary antibody at 4°C overnight, followed by goat anti-rabbit secondary antibody at room temperature for 1 h. After DAPI nuclear staining (10 min) and final PBS washing, anti-fade mounting medium was applied under dim light. CD206 expression was analyzed using laser scanning confocal microscopy .

2.4 Statistical analysis

All experimental data are presented as mean \pm standard deviation (SD) from three independent replicates ($n = 3$). Statistical analyses were performed using *GraphPad Prism 8.0* and *OriginPro 2023*. For two-group comparisons, Student's t-test was applied, while analysis of variance (ANOVA) was used for multi-group comparisons. Statistical significance thresholds were defined as: * $p < 0.05$, ** $p < 0.01$, *** $p < 0.001$, **** $p < 0.0001$; ns (not significant) = $p \geq 0.05$.

3 Results

3.1 Molecular Docking Analysis

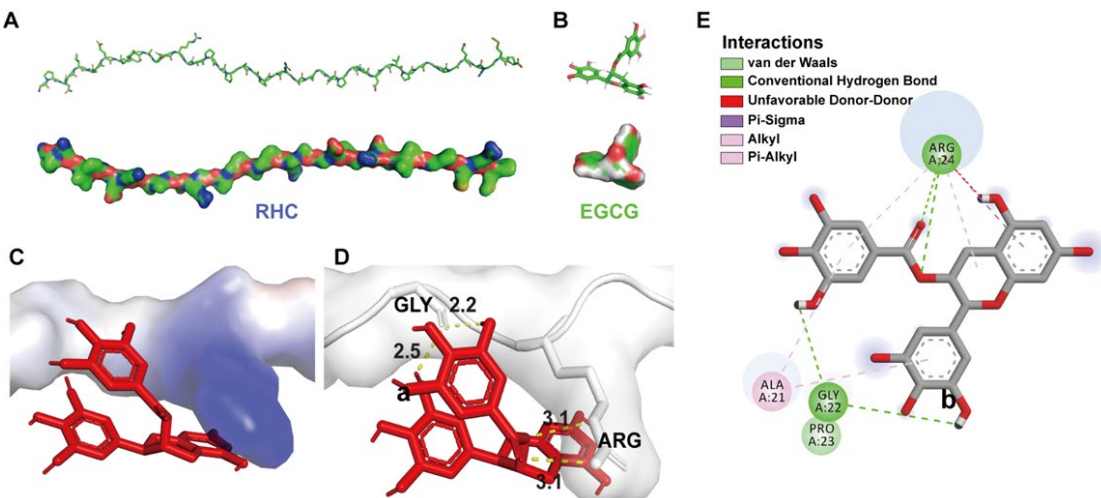


Figure 1. Figure1. Molecular Docking Analysis of EGCG-RHC interactions. (A) Structural models of recombinant human collagen (RHC) with characteristic Gly-XY repeating units and Three-dimensional conformation of EGCG (B) showing hydroxyl group spatial arrangement. (C) Molecular dynamics-derived surface representation: RHC (gray surface) and EGCG (red stick model). Electrostatic potential mapping of binding interface (color scale: red = -5 kT/e, blue = +5 kT/e) with EGCG docked in optimal orientation. (D) Binding pocket analysis showing hydrogen bonding network (red dashed lines, 2.2-3.1 Å) between EGCG's hydroxyl groups (O2/O3) and RHC residues Arg/Gly. (E) Two-dimensional ligand interaction diagram illustrating key contacts: Hydrogen bonds (green arrows), hydrophobic interactions (pink spheres).

By engineering polyphenols with functional and interacting components to enhance their stability, which can be effectively address cellular uptake, and target-specific delivery^[16]. The physical and chemical properties of polyphenols can be systematically modified through engineering to achieve desired characteristics. Molecular docking serves as an effective method for studying protein-ligand interactions^[17]. In this study, we obtained the amino acid residues, hydrogen bond counts, and interaction distances for the EGCG-RHC interaction by selecting the protein-polyphenol conformation with the lowest energy score, as this represents the most probable interaction mode. Figure 1A,B illustrated the rod-like and three-dimensional structures of RHC and EGCG. Figure 1C presented a preliminary electrostatic map of the docking site of RHC and EGCG, suggesting that polyphenol molecules may interact with specific regions of the protein surface. Figures 1D and 1E depicted the interaction between EGCG and the carboxyl groups of the amino acid residues Arg and Gly of RHC, where four hydrogen bonds are formed with lengths ranging from 2.2 to 3.1 Å. These findings indicated that the hydroxyl groups in the EGCG structure could establish hydrogen bonds with the surface residues of RHC. Additionally, RHC exhibited the characteristics of Gly-XY, where Gly, as the largest amino acid residue, provided ample hydrophobic regions for recombinant collagen, thereby creating a favorable environment for the interaction between EGCG and recombinant collagen. Molecular docking analysis revealed that the optimal binding energy of

EGCG and RHC was -4.1 kcal/mol, indicating that EGCG and RHC can interact spontaneously, thereby providing a molecular basis for their binding.

3.2 Preparation and characterization of EGCG-RHC SNs

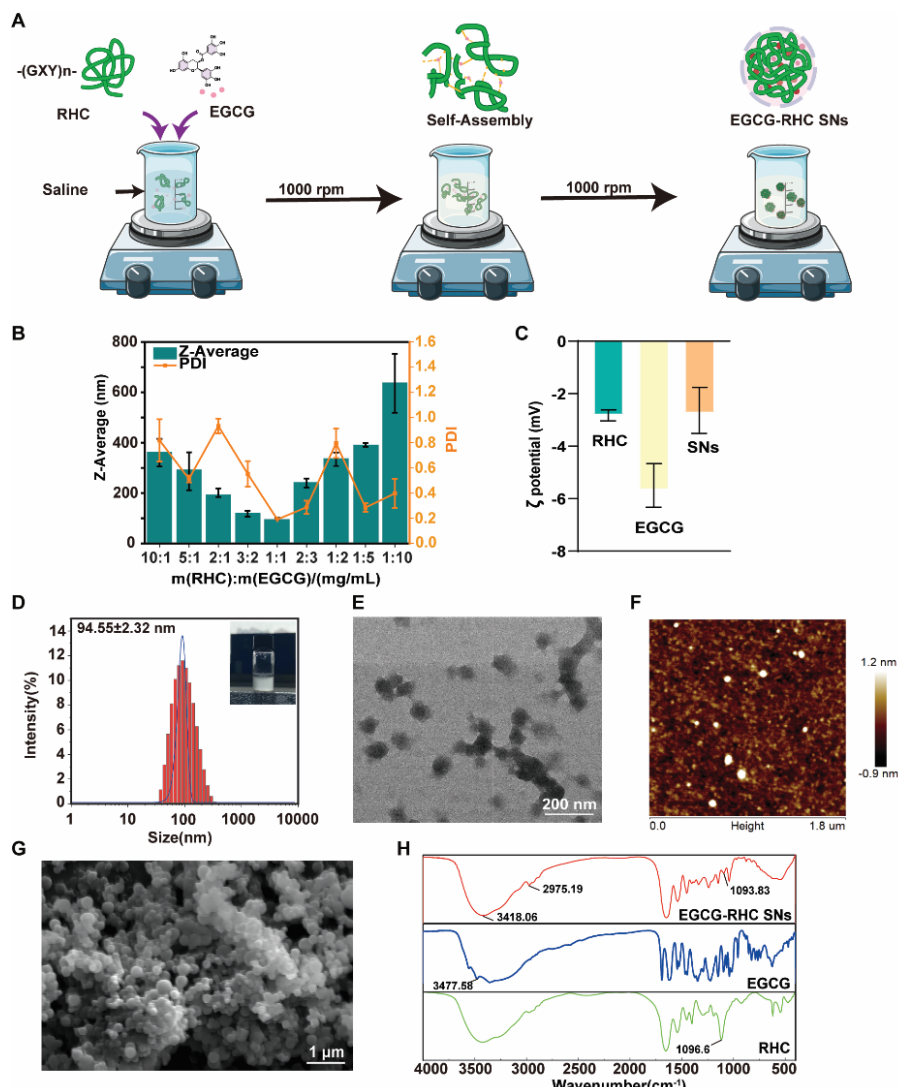


Figure 2. Preparation and multiscale characterization of EGCG-RHC self-assembled nanoparticles (SNs).

(A) Schematic representation of the self-assembly process driven by molecular interactions between RHC and EGCG polyphenols. (B) Influence of the ratio of the mass concentrations of RHC and EGCG on the mean particle size and PDI of EGCG-RHC SNs. (C) ζ potential of RHC, EGCG and EGCG-RHC SNs. (D) Colloidal properties: Hydrodynamic diameter distribution ($Z\text{-average} = 94.55 \pm 2.32$ nm, PDI = 0.18; n=3 independent batches) with inset showing Tyndall effect in corresponding colloidal suspension. (E) Transmission electron microscopy (TEM) analysis of EGCG-RHC SNs with scale bar = 200 nm. (F) Atomic force microscopy (AFM) phase image revealing surface topology. (G) Scanning electron microscopy (SEM) analysis of EGCG-RHC SNs with scale bar = 1 μ m. (H) Comparative FTIR spectroscopy (ATR mode, 4000-400 cm^{-1}) .

The EGCG-RHC self-assembled nanospheres (SNs) were fabricated via a one-step assembly strategy in physiological saline (Figure 2A). Rapid mixing of clear EGCG and RHC solutions triggered spontaneous self-assembly driven by protein-polyphenol interactions,

yielding stable nanospheres. Given the critical role of nanoparticle size (10-100 nm) in transdermal delivery performance^[18], systematic optimization was performed by monitoring particle size variations across concentration ratios.

Dynamic laser scattering (DLS) technology was utilized to characterize the self-assembled nanospheres formed by the combination of EGCG and RHC at different concentration ratios (Figure 2B). When the concentration ratio of EGCG to RHC is 1:1, the average particle size of the prepared EGCG-RHC SNs is minimized, exhibiting good dispersion (PDI < 0.2). Therefore, we selected a concentration ratio of 1:1 for EGCG to RHC as the optimal formulation for the preparation of EGCG-RHC SNs. The zeta potential measurements revealed surface charge alignment between EGCG-RHC SNs (-2.74 ± 0.71 mV) and RHC (-2.82 ± 0.17 mV), suggesting RHC-dominated surface composition (Figure 2C).

The resultant suspension displayed slight opalescence, producing SNs with minimal hydrodynamic diameter (94.55 ± 2.32 nm) and narrow polydispersity (PDI < 0.2) (Figure 2D). Morphological characterization demonstrated spherical nanoparticles with size discrepancies between techniques: TEM/AFM revealed dehydrated particles of 60-70 nm (Figure 2E,F), whereas SEM showed 70 nm spheres with freeze-drying-induced aggregation (Figure 2G). This 30% size reduction compared to DLS data (94.55 nm) reflects hydration shell loss during drying.

FTIR spectral analysis (Figure 1H) confirmed molecular interactions through three key observations: (1) Red-shifted aromatic vibrations (1527-1692 cm⁻¹) with peak broadening indicated EGCG encapsulation; (2) Hydroxyl peak displacement (3477.58 → 3418.06 cm⁻¹) demonstrated hydrogen bonding; (3) Emerging C-H stretching (2975.19 cm⁻¹) and shifted C-O vibration (1096.6 → 1093.83 cm⁻¹) revealed hydrophobic and π-π interactions. These non-covalent binding mechanisms correlated with molecular docking predictions.

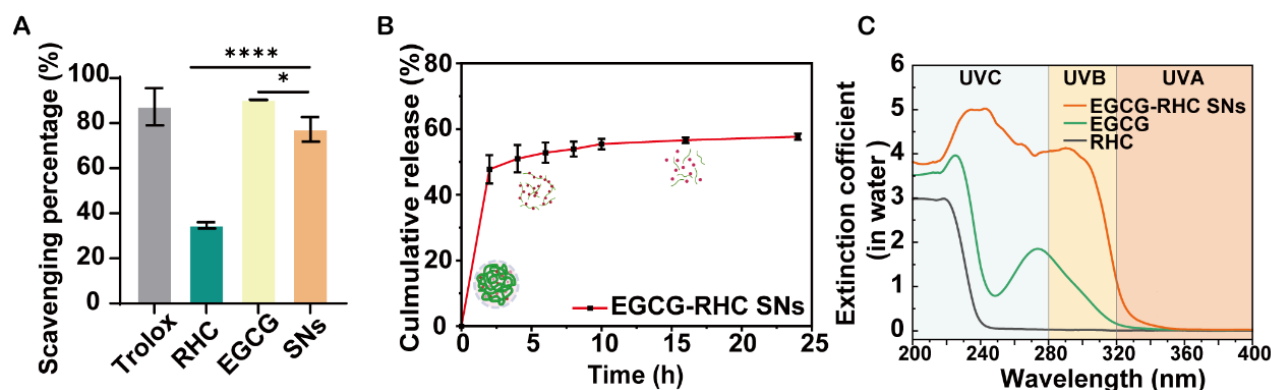
3.3 Functional Characterization of EGCG-RHC SNs: Antioxidant Capacity, Controlled Release, and Ultraviolet Extinction Capability

EGCG, a potent antioxidant, is capable of effectively scavenging reactive oxygen species (ROS)^[5]. To determine whether the self-assembly process of EGCG with RHC affects the antioxidant capacity of EGCG, in vitro antioxidant capacity of EGCG-RHC SNs was assessed using the DPPH free radical scavenging assay. Figure 3A indicated that the DPPH free radical scavenging ability of EGCG-RHC SNs was significantly lower than that of EGCG alone. It was primarily attributed to the encapsulation of EGCG by RHC, which limited the interaction between EGCG and the external environment, thereby decreasing the DPPH scavenging activity of EGCG-RHC SNs. Additionally, EGCG-RHC SNs exhibited a high in vitro antioxidant capacity, without significant difference observed compared to the Trolox as positive control group. DPPH assay suggested that the self-assembly process of EGCG and RHC preserved the antioxidant capacity of EGCG.

The encapsulation efficiency of bioactive ingredients is a critical factor influencing their functional performance^[19]. The release behavior of EGCG from EGCG-RHC SNs were investigated in vitro. Figure 2B demonstrated that EGCG could be sustainably released from these nanoparticles. The release profile was characterized by two distinct phases: an initial burst within the first 5 hours, followed by a prolonged slow release phase extending up to 24

hours. This phenomenon was primarily attributed to the initial encapsulation of EGCG on the particle surface, coupled with the subsequent slow release from the rigid core of EGCG-RHC SNs. Notably, the cumulative release rate of EGCG from EGCG-RHC SNs can reach $60.8 \pm 1.2\%$ after 24 hours. Given their high encapsulation efficiency and sustained release capability, EGCG-RHC SNs could deliver elevated concentrations of EGCG to localized sites, facilitating controlled release. Upon reaching the site of action, EGCG-RHC SNs gradually release EGCG, thereby prolonging the presence of EGCG at the target site through sustained release.

Ultraviolet extinction capability refers to a material's ability to extinguish light at specific ultraviolet wavelengths^[20]. A higher extinction coefficient indicates a stronger capacity of the material to absorb, scatter, or reflect light, resulting in a reduction of light energy as it passes through the object. The UV spectrum of EGCG-RHC SNs was measured in the 200-600 nm range to evaluate their UV extinction capability. The results, illustrated in the figure 2C, showed that both EGCG and EGCG-RHC exhibited similar absorption peaks at 220 nm and 276 nm, but did not demonstrate significant absorption in the UVA region. In contrast to EGCG, the self-assembly of EGCG and RHC into nanospheres led to a broader absorption range in the UVB region. This enhancement was likely due to the inherent absorption properties of EGCG molecules combined with scattering effects associated with the nanosphere morphology. These findings indicated that EGCG-RHC SNs possessed broader UV extinction capabilities,



highlighting their potential application as UVB filters.

Figure 3. Functional evaluation of EGCG-RHC SNs. (A) DPPH radical scavenging activity of experimental groups. (B) In vitro release kinetics of EGCG from SNs (mean \pm SD, n = 3). (C) UV-Vis absorption spectra of aqueous solutions.

3.4 Enhanced Repair of Oxidative Damage in UVB-Induced Photoaging Model by EGCG-RHC SNs

The epidermis plays a pivotal role in both the initiation and recovery of skin damage induced by UVB radiation^[21]. As human immortalized keratinocytes closely mimic epidermal responses, HaCaT cells were selected for this study. Cells were irradiated with narrowband UVB ($30 \text{ mW/cm}^2 \times 360 \text{ s} = 120 \text{ mJ/cm}^2$) to establish photodamage (Figure 5A). Morphological analysis revealed characteristic UV-induced changes: 53.2% of cells exhibited rounded morphology with filopodia retraction and partial detachment from culture substrate (Figure 5A).

CCK-8 viability assays confirmed a significant reduction in survival rate (63.96% vs control) post-irradiation (Figure S2). To balance experimental validity and cell viability, 120 mJ/cm² (6 min irradiation) was selected as the optimal photoaging induction parameter.

Next, the treatment of UVB-induced photodamaged HaCaT cells was conducted using EGCG, RHC, and EGCG-RHC SNs. Cell viability, colony formation, and scratch migration assays were employed to evaluate their efficacy in restoring cell viability and promoting cell proliferation. The results, as shown in the figure 5B, indicated that at a concentration of 10 µg/mL, EGCG-RHC SNs significantly enhanced cell viability following UVB-induced damage compared to the model group, whereas individual treatments with EGCG and RHC did not demonstrate a notable effect. Cell proliferation and migration are crucial for the damage repair process^[22]. Results depicted in the figure 5C and 5D indicated that the number of cell clones in the Model group was significantly reduced compared to the Control group, reflecting a marked decrease in cell proliferation ability. Following the administration of RHC, EGCG, and EGCG-RHC SNs, the number of cell clones increased, and the cell proliferation ability was partially restored in comparison to the Model group. Notably, the number of cell clones in the EGCG-RHC SNs group was significantly higher than that in the RHC and EGCG groups, suggesting that EGCG-RHC SNs could partially reverse UV damage and promote the recovery of cell proliferation ability. Additionally, cell migration experiments (Figure 5E,F) revealed that the migration rate of HaCaT cells was significantly diminished after UVB irradiation. However, in comparison to the Model group, EGCG-RHC SNs significantly restored cell migration ability, outperforming the treatments with EGCG and RHC alone.

The observed functional recovery prompted an investigation into the molecular mechanisms underlying UVB damage repair. Previous studies have indicated that continuous exposure to UVB radiation triggers the production of reactive oxygen species (ROS), leading to cell apoptosis and ultimately resulting in photoaging and skin inflammation^[23]. Notably, EGCG-RHC SNs demonstrated superior repair effects compared to RHC and EGCG alone, likely due to their enhanced cellular uptake, which facilitates the scavenging of intracellular ROS. Consequently, we further investigated the repair mechanism of EGCG-RHC SNs. Fluorescence microscopy was employed to evaluate the ROS levels in photodamaged cells treated with RHC, EGCG, and EGCG-RHC SNs. As shown in Figure 5G, ROS levels in HaCaT cells increased significantly following UVB irradiation. Importantly, compared to the Model, all other treatment groups exhibited clear ROS scavenging capabilities, with EGCG-RHC SNs showing the highest ROS scavenging efficiency (Figure 5H).

Mitochondria serve as a significant source of intracellular reactive oxygen species (ROS) production and are also a primary target vulnerable to ROS-induced damage^[21]. The generation of ROS can lead to a reduction in mitochondrial membrane potential (MMP)^[24]. As illustrated in Figure 5I, the ratio of JC-1 aggregates to monomers in the administration groups

was higher compared to the Model group, indicating a recovery of mitochondrial membrane potential. Importantly, the restoration of mitochondrial membrane potential by EGCG-RHC SNs was significantly greater than that observed in the RHC and EGCG-treated groups (Figure 5J). These findings suggested that EGCG-RHC SNs were effective in reversing the decline in mitochondrial membrane potential caused by ROS and in mitigating UVB-induced mitochondrial damage.

4 Discussion

Epigallocatechin gallate (EGCG) is a significant polyphenol found in green tea, reportedly exhibiting the highest concentration (50-70%) and demonstrating the strongest biological activity among its counterparts^[25]. Research indicates that EGCG possesses a variety of biological activities that may confer health benefits, including antioxidant^[26], antibacterial^[27], anti-obesity^[28], anti-inflammatory^[29], anticancer^[30], cardiovascular protective^[29], and neuroprotective effects^[31]. The biological activity of EGCG surpasses that of many other polyphenols, which can be attributed to the abundance of hydroxyl groups on the aromatic ring and their unique distribution pattern. However, the application of EGCG as a health-promoting agent is often limited by its poor stability under alkaline and neutral conditions, leading to chemical degradation and a consequent reduction in biological activity^[32].

Protein modification through the interaction of polyphenols and proteins has emerged as a promising strategy for fabricating novel protein conjugates with enhanced antioxidant activity^[17]. Polyphenols exhibit binding affinities to proteins via non-covalent and/or covalent interactions, thereby providing a method for engineering polyphenol-protein complexes that protect against oxidation and enzymatic hydrolysis^[15]. Recent studies have reported the development of protein-polyphenol complexes and conjugates that significantly differ in structure and physicochemical properties, enhancing antioxidant activity^[33]. Collagen is the most abundant protein in the extracellular matrix (ECM), providing essential structural support and elasticity^[34]. In this study, recombinant humanized type III collagen (RHC) was engineered as a structural protein matrix to encapsulate EGCG. We initially employed molecular docking to simulate and evaluate the interaction between EGCG and RHC. The results indicated that EGCG possesses a strong binding affinity for RHC, establishing a theoretical foundation for the engineering of EGCG and RHC. Furthermore, we conducted a preliminary investigation into the binding mechanism of EGCG-RHC SNs using infrared spectroscopy, revealing that EGCG and RHC are primarily bound through non-covalent interactions, including hydrogen bonds and hydrophobic interactions. Additionally, EGCG-RHC SNs maintain the antioxidant activity of EGCG, while enabling a controlled release over an extended period, both of which significantly enhance their bioavailability.

Nanomaterials, particularly those with dimensions less than 100 nm, have demonstrated

the ability to traverse the stratum corneum of the skin through various mechanisms, thereby facilitating transdermal delivery^[35]. However, there are notable limitations to the transdermal absorption of collagen, primarily due to its molecular characteristics and the structural properties of the skin^[36]. Significant challenges include the high molecular weight of collagen, which often exceeds 50 kDa, making it difficult for these large molecules to penetrate the stratum corneum, the outermost layer of the skin^[37]. This barrier is composed of tightly packed keratinocytes and lipids, which effectively restrict the passage of larger molecules such as collagen. The stratum corneum serves as a formidable barrier to drug absorption, and its hydrophobic nature further complicates the transdermal delivery of hydrophilic substances like collagen. The molecular size and hydrophilicity of collagen limit its ability to diffuse through the lipid-rich interstitial spaces in the stratum corneum, which is the primary pathway for transdermal absorption^[38]. Consequently, only a small proportion of topically applied collagen reaches the deeper layers of the skin to exert its beneficial effects.

The antioxidant activity of protein-polyphenol complexes and conjugates has been investigated through various in vitro assays^[39]. Generally, polyphenols exhibited higher antioxidant potential than their corresponding protein conjugates, which, in turn, demonstrated greater antioxidant activity than proteins alone^[17]. Polyphenols with a high reactive hydroxyl content, such as EGCG, formed protein complexes and conjugates that possessed higher antioxidant activity compared to polyphenols with lower hydroxyl content^[15]. In our study, we evaluated the antioxidant capacity of EGCG-RHC SNs in vitro using the DPPH assay. The results indicated that the antioxidant capacity of EGCG alone surpassed that of the EGCG-RHC SN complex. However, in the HaCat cell photoaging model, the ROS scavenging ability of EGCG-RHC SNs was significantly superior to that of EGCG, suggesting enhanced antioxidant properties. These findings aligned with existing literature, which indicated that EGCG tends to exhibit a direct burst release effect when administered alone, while EGCG-RHC SNs demonstrated a sustained indirect effect due to their excellent sustained release characteristics. This discrepancy helps to explain the inconsistent results observed in various experiments regarding the antioxidant capacity of EGCG-RHC SNs.

Nonetheless, we demonstrated that EGCG-RHC SNs could inhibit UVB-induced oxidative stress and reduce ROS production, thereby further mitigating the inflammatory response and apoptosis. Our findings supported the potential application of EGCG-RHC SNs in preventing UVB-induced photodamage and in the development of cosmetic ingredients aimed at preventing UVB-induced skin damage.

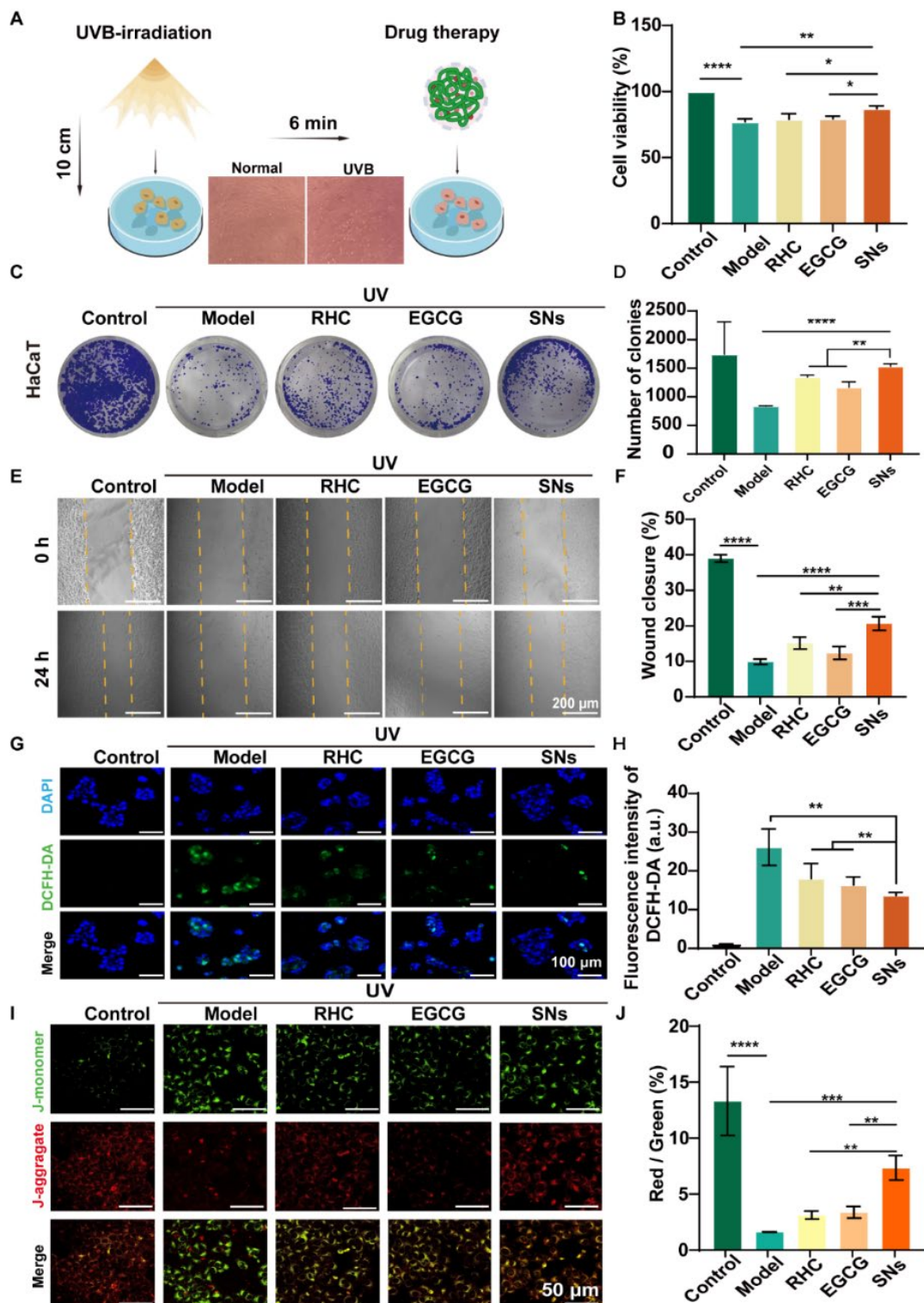


Figure 4. EGCG-RHC SNs repair UVB-induced photodamage in HaCaT keratinocytes. (A) Schematic workflow for evaluating UVB damage repair: (Top) Experimental timeline of UVB irradiation (30 mJ/cm^2) and treatment; (Bottom) Morphological changes of HaCaT cells pre/post-UVB exposure. (B) Cell viability quantified by CCK-8 assay ($n=6$), demonstrating UV-protective capacity. (C) Colony formation assay showing proliferative recovery. (D) Quantitative analysis of colony counts ($n=3$). (E) Scratch wound healing assay in NIH-3T3 fibroblasts. (F) Quantified residual wound width ($n=3$). (G) Intracellular ROS levels detected by DCFH-DA fluorescence (green). (H) Normalized fluorescence intensity ($n=3$). (I) JC-1 staining

showing mitochondrial membrane potential (red: J-aggregates; green: monomers). (J) J-aggregate/monomer ratio quantification ($n=3$). Scale bars: 100 μm (A,E), 50 μm (G,I). All data presented as mean \pm SD. * $p<0.05$, ** $p<0.01$ vs Model group.

5 Conclusion

In this study, we employed a straightforward and practical self-assembly strategy to develop EGCG-RHC SNs. EGCG-RHC SNs not only addressed the issue of low bioavailability of EGCG in practical applications but also enhanced the transdermal absorption efficiency of recombinant type III humanized collagen. These nanoparticles exhibited robust antioxidant, anti-inflammatory, and sustained-release properties. EGCG-RHC SNs contribute to the amelioration of photoaging and the prevention of UVB-induced oxidative and inflammatory responses, as an effective approach to prevent and mitigate skin photoaging induced by UVB radiation. Their therapeutic efficacy surpassed that of any individual component used in isolation. Furthermore, our results highlighted the significance of the complex formed through the interaction between polyphenols and proteins in enhancing the practical applicability of polyphenols and functional proteins, thereby offering promising opportunities for the use of polyphenolic antioxidants and recombinant type III collagen in pharmaceutical and cosmetic applications.

6 References

- [1] P. Sharma, T. Dhiman, R. S. Negi, A. Oc, K. Gupta, J. S. Bhatti, S. Thareja, *South African Journal of Botany* **2024**, 166, 466.
- [2] M. C. McCabe, R. C. Hill, K. Calderone, Y. Cui, Y. Yan, T. Quan, G. J. Fisher, K. C. Hansen, *Matrix Biology Plus* **2020**, 8, 100041.
- [3] J. Wang, H. Qiu, Y. Xu, Y. Gao, P. Tan, R. Zhao, Z. Liu, Y. Tang, X. Zhu, C. Bao, H. Wang, H. Lin, X. Zhang, *Bioactive Materials* **2022**, 11, 154.
- [4] L. Cao, Z. Zhang, D. Yuan, M. Yu, J. Min, *Front. Bioeng. Biotechnol.* **2024**, 12.
- [5] X. Peng, D. J. McClements, X. Liu, F. Liu, *Critical Reviews in Food Science and Nutrition* **2024**, 0, 1.
- [6] Y. Guo, Q. Sun, F.-G. Wu, Y. Dai, X. Chen, *Advanced Materials* **2021**, 33, 2007356.
- [7] R. Sahadevan, Singh ,Satyam, Binoy ,Anupama, S. and Sadhukhan, *Critical Reviews in Food Science and Nutrition* **2023**, 63, 10382.
- [8] J. Shi, M. Zhang, L. Zhang, H. Deng, *Environmental Pollution* **2018**, 239, 466.
- [9] R. Sahadevan, S. Singh, A. Binoy, S. Sadhukhan, *Critical Reviews in Food Science and Nutrition* **2023**.
- [10] L. Ma, Y. Tan, Q. Tong, X. Cao, D. Liu, X. Ma, X. Jiang, X. Li, *Advanced Healthcare Materials* **2024**, 13, 2303297.
- [11] P. Bakun, D. T. Mlynarczyk, T. Koczorowski, M. Cerbin-Koczorowska, L. Piwowarczyk, E.

- Kolasiński, M. Stawny, J. Kuźmińska, A. Jelińska, T. Goslinski, *European Journal of Medicinal Chemistry* **2023**, 261, 115820.
- [12] Y. Kim, Y. Baek, E. Jeong, H. G. Lee, *Colloids and Surfaces B: Biointerfaces* **2024**, 234, 113723.
- [13] C. Ke, X. Yang, L. Li, *Food Chemistry* **2025**, 144444.
- [14] H. Li, M. Yang, Y. Jia, R. Dai, X. Wang, Y. Han, W. Lei, Z. Gao, *Food Chemistry* **2025**, 144436.
- [15] X. Sun, R. A. Sarteshnizi, C. C. Udenigwe, *Current Opinion in Food Science* **2022**, 45, 100840.
- [16] Y. Han, R. P. M. Lafleur, J. Zhou, W. Xu, Z. Lin, J. J. Richardson, F. Caruso, *Journal of the American Chemical Society* **2022**.
- [17] Y. Li, D. He, B. Li, M. N. Lund, Y. Xing, Y. Wang, F. Li, X. Cao, Y. Liu, X. Chen, J. Yu, J. Zhu, M. Zhang, Q. Wang, Y. Zhang, B. Li, J. Wang, X. Xing, L. Li, *Trends in Food Science & Technology* **2021**, 110, 470.
- [18] Y. Li, J. A. Champion, *Advanced Drug Delivery Reviews* **2022**, 189, 114462.
- [19] S. S. Marques, M. A. Segundo, *TrAC Trends in Analytical Chemistry* **2024**, 174, 117672.
- [20] Q. Tong, Y. Xiao, Z. Yi, X. Chen, X. Jiang, X. Li, *Green Chem.* **2023**, 25, 4387.
- [21] L. Li, Y. Liu, R. Chang, T. Ye, Z. Li, R. Huang, Z. Wang, J. Deng, H. Xia, Y. Yang, Y. Huang, *Antioxidants* **2024**, 13, 1002.
- [22] Y. Xie, J. He, S. Li, X. Chen, T. Zhang, Y. Zhao, Y. Lin, X. Cai, *Advanced Functional Materials* **2023**, 33, 2303580.
- [23] X. Yan, Y. Xu, T. Wei, Y. Chai, Y. Li, C. Wang, M. Li, S. Zhang, W. Zhu, Z. Liu, *Adv Funct Materials* **2024**, 2409416.
- [24] L. M. Das, A. M. Binko, Z. P. Traylor, H. Peng, K. Q. Lu, *Autophagy* **2019**, 15, 813.
- [25] N. Khan, H. Mukhtar, *Nutrients* **2018**, 11, 39.
- [26] K. Yokotani, K. Umegaki, *Free Radic Res* **2017**, 51, 193.
- [27] S. Lee, G. S. A. Razqan, D. H. Kwon, *Phytomedicine* **2017**, 24, 49.
- [28] W. Zhan, Y. Liu, D. Li, Y. Liu, *RSC Advances* **2016**, 6, 96918.
- [29] F. Huang, J. Ding, L. Miao, Y. Zhao, F. Wang, *International Journal of Clinical and Experimental Pathology* **2017**, 10, 5580.
- [30] R.-Y. Gan, H.-B. Li, Z.-Q. Sui, H. Corke, *Crit Rev Food Sci Nutr* **2018**, 58, 924.
- [31] L. Xicota, J. Rodriguez-Morato, M. Dierssen, R. de la Torre, *Curr Drug Targets* **2017**, 18, 174.
- [32] X. Peng, McClements ,David Julian, Liu ,Xuebo, F. and Liu, *Critical Reviews in Food Science and Nutrition* **2025**, 65, 2177.
- [33] C. Li, L. Chen, D. J. McClements, X. Peng, Z. Xu, M. Meng, H. Ji, C. Qiu, J. Long, Z. Jin, .
- [34] S. Wei, Z. Li, H. Xia, Z. Wang, J. Deng, L. Li, R. Huang, T. Ye, Y. Huang, Y. Yang, *International Journal of Biological Macromolecules* **2024**, 268, 131723.
- [35] Y. Zhang, W. Ng, X. Feng, F. Cao, H. Xu, *International Journal of Pharmaceutics* **2017**, 516, 225.
- [36] S. Münch, J. Wohlrab, R. H. H. Neubert, *European Journal of Pharmaceutics and Biopharmaceutics* **2017**, 119, 235.

- [37] B. An, Y.-S. Lin, B. Brodsky, *Advanced Drug Delivery Reviews* **2016**, 97, 69.
- [38] M. I. Avila Rodríguez, L. G. Rodríguez Barroso, M. L. Sánchez, *J Cosmet Dermatol* **2018**, 17, 20.
- [39] Y.-C. Chen, S.-H. Yu, G.-J. Tsai, D.-W. Tang, F.-L. Mi, Y.-P. Peng, *Novel Technology for the Preparation of Self-Assembled Catechin/Gelatin Nanoparticles and Their Characterization*, American Chemical Society **2010**.